Inorg. Chem. **2006**, *45*, 5841–5851

Photoelectron Spectroscopy of the Bis(dithiolene) Anions $[M(mnt)_2]^{n-}$ (M = Fe – Zn; n = 1, 2): Changes in Electronic Structure with Variation of Metal Center and with Oxidation

Tom Waters, Xue-Bin Wang, Hin-Koon Woo, and Lai-Sheng Wang*

Contribution from the Department of Physics, Washington State University, 2710 University Drive, Richland, Washington 99354, and Chemical Sciences Division, MS K8-88 Pacific Northwest National Laboratory, P.O. Box 999, Richland, Washington 99352

Received February 14, 2006

A detailed understanding of the electronic structures of transition metal bis(dithiolene) centers is important in the context of their interesting redox, magnetic, and optical properties. The electronic structures of the series $[M(mnt)_2]^{n-}$ (M = Fe – Zn; mnt = 1,2-$S_2C_2(CN)_2$; n = 1, 2) were examined by a combination of photodetachment photoelectron spectroscopy and density functional theory calculations, providing insights into changes in electronic structure with variation of the metal center and with oxidation. Significant changes were observed for the dianions $[M(mnt)_2]^{2-}$ due to stabilization of the metal 3d levels from Fe to Zn and the transition from square-planar to tetrahedral coordination about the metal center (Fe–Ni, D_{2h} → Cu D_2 → Zn, D_{2d}). Changes with oxidation from $[M(mnt)_2]^{2-}$ to $[M(mnt)_2]^{1-}$ were largely dependent on the nature of the redox-active orbital in the couple $[M(mnt)_2]^{2-/1-}$. In particular, the first detachment feature for $[Fe(mnt)_2]^{2-}$ originated from a metal-based orbital (Fe^{II} → Fe^{III}) while that for $[Fe(mnt)_2]^{1-}$ originated from a ligand-based orbital, a consequence of stabilization of Fe 3d levels in the latter. In contrast, the first detachment feature for both of $[Ni(mnt)_2]^{2-}$ and $[Ni(mnt)_2]^{1-}$ originated from the same ligand-based orbital in both cases, a result of occupied Ni 3d levels being stabilized relative those of Fe 3d and occurring below the highest energy occupied ligand-based orbital for both of $[Ni(mnt)_2]^{2-}$ and $[Ni(mnt)_2]^{1-}$. The combined data illustrate the subtle interplay between metal- and ligand-based redox chemistry in these species and demonstrate changes in their electronic structures with variation of metal center, oxidation, and coordination geometry.

Introduction

Transition metal bis(dithiolene) centers have been extensively studied due to their interesting redox, magnetic, optical and conducting properties, and their complex and unusual electronic structures.[1−6] Previous studies have demonstrated that the frontier metal- and ligand-based orbitals occur at similar energies, allowing for significant mixing and resulting in a highly covalent bonding scheme.[6,7] These similar energies can also introduce ambiguity with the assignment of physical oxidation states (i.e., dithiolenes are redox noninnocent ligands[8]), and allow for different descriptions of bonding and interpretation of spectroscopic data.[6,8−14]

* To whom correspondence should be addressed. E-mail: ls.wang@pnl.gov.

(1) Stiefel, E. I., Ed. Dithiolene Chemistry: Synthesis, Properties and Applications. In *Progress in Inorganic Chemistry*; Karlin, K. D., Series Ed.; Wiley: New York, 2003; Vol. 52, p 738.
(2) Mueller-Westerhoff, U.; Vance, B.; Yoon, D. I. *Tetrahedron* **1992**, *47*, 909.
(3) Cassoux, P. *Coord. Chem. Rev.* **1999**, *186*, 213.
(4) Robertson, N.; Cronin, L. *Coord. Chem. Rev.* **2002**, *227*, 93.
(5) Kato, R. *Chem. Rev.* **2004**, *104*, 5319.
(6) Kirk, M. L.; McNaughton, R. L.; Helton, M. E. The Electronic Structure and Spectroscopy of Metallo-Dithiolene Complexes. In *Progress in Inorganic Chemistry*; Karlin, K. D., Series Ed.; Wiley: New York, 2003; Vol. 52, p 111.
(7) Szilagyi, R. K.; Lim, B. S.; Glaser, T.; Holm, R. H.; Hedman, B.; Hodgson, K. O.; Solomon, E. I. *J. Am. Chem. Soc.* **2003**, *125*, 9158.
(8) Ward, M. D.; McCleverty, J. A. *J. Chem. Soc., Dalton Trans.* **2002**, 275.
(9) Stiefel, E. I.; Waters, J. H.; Billig, E.; Gray, H. B. *J. Am. Chem. Soc.* **1965**, *87*, 3016.
(10) Ray, K.; Weyhermüller, T.; Goossens, A.; Craje, M. W. J.; Wieghardt, K. *Inorg. Chem.* **2003**, *42*, 4082.
(11) Sellmann, D.; Geck, M.; Knoch, F.; Ritter, G.; Dengler, J. *J. Am. Chem. Soc.* **1991**, *113*, 3819.
(12) Ray, K.; Bill, E.; Weyhermüller, T.; Wieghardt, K. *J. Am. Chem. Soc.* **2005**, *127*, 5641.
(13) Ray, K.; Begum, A.; Weyhermüller, T.; Piligkos, S.; van Slageren, J.; Neese, F.; Wieghardt, K. *J. Am. Chem. Soc.* **2005**, *127*, 4403.

10.1021/ic060255z CCC: $33.50
Published on Web 06/29/2006

Changes in electronic structure with variation of the metal center and with oxidation can introduce further complexity. These latter aspects are illustrated by two recent examples from the literature:[12−14] (i) the anions $[Fe(bdt)_2]^{2-}$ and $[Co(bdt)_2]^{1-}$ (bdt = benzene-1,2-dithiolato) are isoelectronic but exhibit significantly different electronic structures and properties;[13] and (ii) two-electron oxidation of $[Fe(bdt)_2]^{2-}$ involves sequential oxidation of the metal and then ligand, while that for $[Ni(bdt)_2]^{2-}$ involves ligand-based redox chemistry in both stages.[12,14]

Gas-phase photodetachment photoelectron spectroscopy (PES) allows the electronic structure of gaseous species to be investigated, providing direct information about molecular orbital (MO) energy levels of the parent species and the ground and excited states of the one-electron detached product species. The coupling of electrospray to PES has allowed a number of negatively charged solution-phase species to be transferred to the gas phase and studied for the first time,[15] including oxo-molybdenum bis(dithiolene) centers,[16,17] and the nickel group bis(dithiolene) series $[M(mnt)_2]^{n-}$ (M = Ni, Pd, Pt; mnt = 1,2-$S_2C_2(CN)_2$; n = 1, 2) that are related to those described herein.[18]

The present account describes a systematic investigation into the electronic structures of the 3d transition metal bis(dithiolene) anions $[M(mnt)_2]^{n-}$ (M = Fe−Zn; mnt = 1,2-$S_2C_2(CN)_2$; n = 1, 2) by a combination of photodetachment PES and density functional theory (DFT) calculations. The electron-withdrawing cyanide substituents on the dithiolene ligand were chosen to ensure that each of the dianions were stable gas-phase species (i.e., stable with respect to electron detachment), thereby allowing access to both the doubly and singly charged anions.[17] The combined experimental and theoretical data provide insight into the MO energy levels of each member of the series $[M(mnt)_2]^{n-}$, and highlights changes in the relative energies of metal- and ligand-based orbitals with variation of metal center, with oxidation and with changes in geometric structure.

Experimental Details

Photoelectron Spectroscopy. PES experiments were carried out on a home-built instrument that couples an electrospray source to a magnetic bottle time-of-flight photoelectron spectrometer. The dianions $[M(mnt)_2]^{2-}$ (M = Fe−Zn) were transferred to the gas phase by the electrospray process from solutions of $(Bu_4N)_2$-$[M(mnt)_2]$ in solvent CH_3CN (~0.1 mg mL^{-1}). The singly charged anions $[M(mnt)_2]^{1-}$ (M = Fe − Cu) were formed by one-electron oxidation of $[M(mnt)_2]^{2-}$ during the electrospray process. $[Zn(mnt)_2]^{1-}$ was not observed experimentally and so is not discussed further.

Experiments were carried out on a newly built instrument that is similar to that described previously[15] but which allows for higher resolution due to a longer electron time-of-flight tube and the ability to cool ions to significantly below room temperature.[19,20] Anions from the source were guided by an RF-only octopole device into a quadrupole mass filter (operated in the RF-only mode in the current experiment) and then guided by a 90° ion bender into a 3D Paul trap that is cooled by a closed-cycle helium refrigerator and was maintained at 70 K during the experiments. The incoming ions were trapped and collisionally cooled with background gas (~1 mTorr N_2) for a period of 20−100 ms (~$2-10 \times 10^3$ collisions) to a nominal temperature of ~70−100 K.[19,20] The ions were pulsed into the extraction zone of a time-of-flight mass spectrometer at a 10-Hz repetition rate. Ions of interest were mass-selected and decelerated before being intercepted by the laser beam (193 nm from an ArF excimer laser or 266 and 355 nm from a Nd:YAG laser) in the interaction zone of the magnetic-bottle photoelectron analyzer. The lasers were operated at a 20 Hz repetition rate with the ion beam off at alternate shots for background subtraction. The photodetached electrons were collected with high efficiency by the magnetic-bottle and analyzed in a 5-m-long electron flight tube. Photoelectron time-of-flight spectra were collected and then converted into kinetic energy spectra, calibrated by the known spectra of I^- and ClO_2^-.[21] Electron binding energy spectra were obtained by subtracting the kinetic energy spectra from the detachment photon energies. Energy resolution ($\Delta E/E$) was estimated as ~2% (fwhm), i.e., ~20 meV for 1 eV electrons, as measured from the spectra of I^- at 355 nm.

Theoretical Calculations. Geometry optimizations and molecular orbital energy levels were calculated at the density functional level of theory using the BP86 functional.[22,23] Calculations employed the 6-311+G* basis sets for C, N, and S, and the Stuttgart quasi-relativistic effective core potentials and basis sets augmented with two f-type and one g-type polarization functions for Fe−Zn.[24,25] Calculations were carried out using the NWChem 4.6 program at the Molecular Science Computing Facility located at the W. R. Wiley Environmental Molecular Sciences Laboratory.[26] Three-dimensional contours of the calculated molecular orbitals were generated using the Extensible Computational Chemistry Environment (Ecce) software.[27]

Geometries for $[M(mnt)_2]^{n-}$ were chosen with guidance from the theoretical calculations and available condensed phase data (see below). Cartesian axes for planar species were chosen such that the molecule lies in the *xy* plane with the *x* axis bisecting the C−C bond of the dithiolene chelate rings. Cartesian coordinates for the optimized geometries for each $[M(mnt)_2]^{n-}$ complex are included in the Supporting Information (Tables S1−S5).

The ground-state electronic structures for each of $[M(mnt)_2]^{n-}$ (n = 0−2) were chosen with guidance from the theoretical calculations and from available condensed phase data (see below).

(14) Ray, K.; Weyhermüller, T.; Neese, F.; Wieghardt, K. *Inorg. Chem.* **2005**, *44*, 5345.
(15) Wang, L. S.; Ding, C. F.; Wang, X. B.; Barlow, S. E. *Rev. Sci. Instrum.* **1999**, *70*, 1957.
(16) Wang, X. B.; Inscore, F. E.; Yang, X.; Cooney, J. J. A.; Enemark, J. H.; Wang, L. S. *J. Am. Chem. Soc.* **2002**, *124*, 10182.
(17) Waters, T.; Wang, X. B.; Yang, X.; Zhang, L. Y.; O'Hair, R. A. J.; Wang, L. S.; Wedd, A. G. *J. Am. Chem. Soc.* **2004**, *126*, 5119.
(18) Waters, T.; Woo, H. K.; Wang, X. B.; Wang, L. S. *J. Am. Chem. Soc.* **2006**, *128*, 4282.
(19) Wang, X. B.; Woo, H. K.; Kiran, B.; Wang, L. S. *Angew. Chem., Int. Ed.* **2005**, *44*, 4968.
(20) Wang, X. B.; Woo, H. K.; Wang, L. S. *J. Chem. Phys.* **2005**, *123*, 051106.
(21) Gilles, M. K.; Polak, M. L.; Lineberger, W. C. *J. Chem. Phys.* **1992**, *96*, 8012.
(22) Perdew, J. P. *Phys. Rev. B* **1986**, *33*, 8822.
(23) Becke, A. D. *Phys. Rev. A* **1988**, *38*, 3098.
(24) (a) Dolg, M.; Wedig, U.; Stoll, H.; Preuss, H. *J. Chem. Phys.* **1987**, *86*, 866. (b) Andrae, D.; Haeussermann, Y.; Dolg, M.; Stoll, H.; Preuss, H. *Theor. Chim. Acta* **1990**, *77*, 123.
(25) Martin, J. M. L.; Sundermann, A. *J. Chem. Phys.* **2001**, *114*, 3408.
(26) (a) Aprà, E.; et al. *NWChem, A Computational Chemistry Package for Parallel Computers*, Version 4.6; Pacific Northwest National Laboratory: Richland, WA, 2004. (b) Kendall, R. A.; et al. *Comput. Phys. Comm.* **2000**, *128*, 260.
(27) Black, G.; et al. *Ecce, A Problem Solving Environment for Computational Chemistry*, Software Version 3.2.2; Pacific Northwest National Laboratory: Richland, WA, 2005.

Theoretical predictions for the first vertical detachment energies (VDEs) for each of $[M(mnt)_2]^{2-}$ and $[M(mnt)_2]^{1-}$ were calculated by the ΔSCF method, i.e., the difference in energy between the ground states of the parent and one-electron detached species, with the geometry of the one-electron detached species fixed at that of the parent (i.e., vertical detachment). Electron detachment from a range of the highest lying occupied orbitals of $[M(mnt)_2]^{2-}$ and $[M(mnt)_2]^{1-}$ was tested in order to ensure the correct redox-active orbital in the detachment transition was identified, i.e., ensure the lowest energy ground state configuration of the product species. Higher energy features in the photoelectron spectra were qualitatively interpreted in the spirit of Koopmans' theorem on the basis of the predicted orbital energies from the BP86 calculations (Figures 3−7). The use of spin-unrestricted Kohn−Sham orbital energies from DFT calculations has been demonstrated as a reasonable basis for the interpretation of photoelectron spectra of open shell molecules,[28,29] and the approach is intended to provide a first-order framework in which to interpret the experimental data. However, the method does not take into account the effects of electronic relaxation of the final state associated with ionization, and a proper description of such effects would require more detailed calculations on the ground and excited states of the one electron detached species.

Experimental Results

Photoelectron Spectra of the Doubly Charged Anions $[M(mnt)_2]^{2-}$ (M = Fe−Zn). Phtotoelectron spectra of $[M(mnt)_2]^{2-}$ (M = Fe−Zn) were recorded at 193, 266, and 355 nm photon energies (6.424, 4.661, and 3.496 eV, respectively) and are presented in Figure 1. The present account is focused on the highest energy occupied orbitals of $[M(mnt)_2]^{2-}$, and so only the first few detachment features for each species are considered. The first detachment feature is labeled X, and the remaining features are labeled A, B, etc. in order of increasing energy (Figure 1). Adiabatic and vertical detachment energies (ADE and VDE, respectively) are detailed in Table 1. ADEs represent the electron affinities of the corresponding singly charged anions and were measured from the onset of the first detachment feature, while VDEs for each feature were measured from the peak maximum. The difference between the first VDE and ADE for each of $[M(mnt)_2]^{2-}$ provides an indication of the reorganization energy associated with the detachment event, i.e., the energy associated with geometric relaxation following oxidation.[30]

The 266 and 355 nm spectra showed fewer detachment features but have better resolution due to the lower kinetic energies of the photoelectrons. However, these lower-photon-energy spectra were complicated by the fact that many of $[M(mnt)_2]^{2-}$ are strongly absorbing at these wavelengths,[31−33] giving rise to the possibility of autodetachment transitions. These involve resonant photoexcitation to a metastable excited state of the dianion that lies above the ionization threshold, which can undergo vibrational or electronic relaxation prior to electron detachment.[34,35] Such autodetachment processes tend to result in the appearance of broader and non-Franck−Condon features in the lower-photon-energy spectra that are not present in the 193 nm spectra. For example, no detachment features were observed at ∼2.2 eV in the 193 nm spectrum for $[Zn(mnt)_2]^{2-}$ (Figure 1e); however, a broad signal was observed in this region in the 266 nm spectrum and was assigned to an autodetachment transition. Experimental features that are assigned to such autodetachment transitions are labeled with an asterisk in Figure 1 and are not considered further.

The Repulsive Coulomb Barrier. The photoelectron spectra of the dianions $[M(mnt)_2]^{2-}$ are truncated at the higher binding energy side in each experiment due to the repulsive Coulomb barrier (RCB), a general feature of electron detachment from multiply charged anions.[36−39] This barrier to electron detachment arises from the superposition of short-range electron attachment and long-range Coulomb repulsion between the two negatively charged photoproducts (e.g., $A^{2-} \rightarrow A^- + e^-$). The RCB is evident in the experimental spectra by the absence of higher-binding-energy features, which are not observed due to the lower-kinetic-energy electrons having insufficient energy to surmount the barrier.[36−38] The magnitude of the RCB for each of $[M(mnt)_2]^{2-}$ can be estimated from the difference between the photon energy and the spectral cutoff in each case. For example, the 355 and 266 nm spectra for each of the five complexes were cut off at ∼2 and ∼3 eV, respectively (Figure 1). This allowed the RCB to be estimated as ∼1.5 eV for each of $[M(mnt)_2]^{2-}$ (i.e., photon energy − cutoff = 3.496 − 2 and 4.661 − 3 eV, respectively). These similar estimates were consistent with the similar sizes resulting in similar Coulomb repulsion in each case.[37]

$[Fe(mnt)_2]^{2-}$. Two very weak threshold features labeled X and A were observed with VDEs of 0.36 and 0.64 eV, respectively (Figure 1a). These features were observed at each of the three photon energies but were slightly stronger at 266 nm (Figure 1a, inset). These weak features were consistently observed in multiple experiments and are assigned as real detachment features from $[Fe(mnt)_2]^{2-}$. Feature B appears as a shoulder on the low-binding-energy side of feature C and was more clearly resolved at 266 nm. Feature C exhibits some vibrational structure at 355 nm (∼800 cm^{-1}), while the feature at ∼1.8 eV also exhibits vibrational structure in the 266 nm spectrum (∼1200 cm^{-1}). This vibrational structure is expected to arise from vibrational modes of the dithiolene ligand backbone.

$[Co(mnt)_2]^{2-}$. The first band for $[Co(mnt)_2]^{2-}$ in the 193 nm spectrum contains two overlapping features X and A that

(28) (a) Gritsenko, O. V.; Baerends, E. J. *J. Chem. Phys.* **2002**, *117*, 9154. (b) Gritsenko, O. V.; Baerends, E. J. *J. Chem. Phys.* **2004**, *120*, 8364.
(29) Hamel, S.; Duffy, P.; Casida, M.; Salahub, D. R. *J. Electron Spectrosc. Relat. Phenom.* **2002**, *123*, 345.
(30) Wang, X. B.; Wang, L. S. *J. Chem. Phys.* **2000**, *112*, 6959.
(31) Shupack, S. I.; Billig, E.; Clark, R. J. H.; Williams, R.; Gray, H. B. *J. Am. Chem. Soc.* **1964**, *86*, 4594.
(32) Chandramouli, G. V. R.; Manoharan, P. T. *Inorg. Chem.* **1986**, *25*, 4680.
(33) Persaud, L.; Langford, C. H. *Inorg. Chem.* **1985**, *24*, 3562.
(34) Wang, X. B.; Ding, C. F.; Wang, L. S. *J. Chem. Phys.* **1999**, *110*, 8217.
(35) Li, J.; Li, X.; Zhai, H. J.; Wang, L. S. *Science* **2003**, *299*, 864.
(36) Wang, X. B.; Ding, C. F.; Wang, L. S. *Phys. Rev. Lett.* **1998**, *81*, 3351.
(37) Wang, L. S.; Ding, C. F.; Wang, X. B.; Nicholas, J. B. *Phys. Rev. Lett.* **1998**, *81*, 2667.
(38) Wang, L. S.; Wang, X. B. *J. Phys. Chem. A* **2000**, *104*, 1978.
(39) Dreuw, A.; Cederbaum, L. S. *Chem. Rev.* **2002**, *102*, 181.

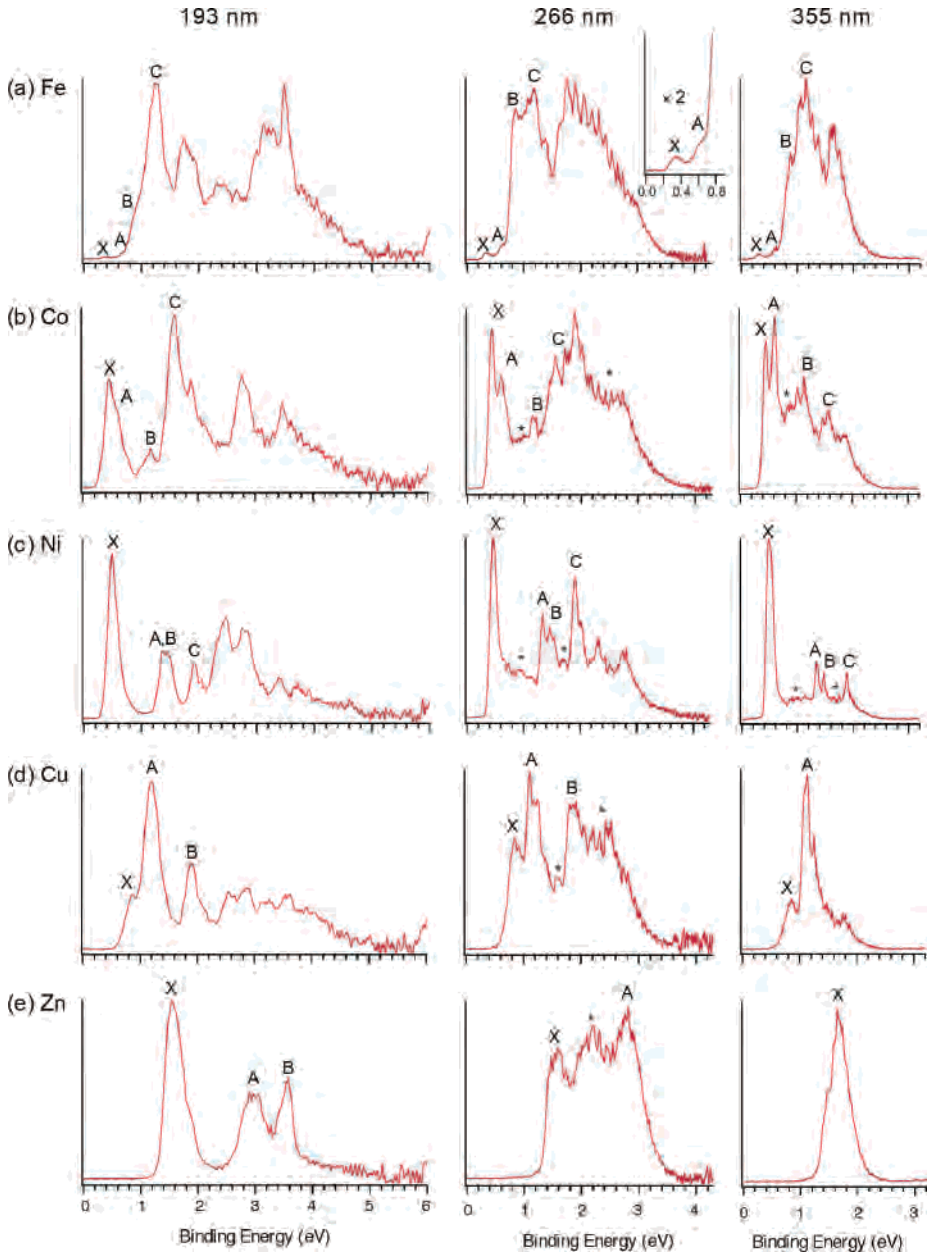

Figure 1. Photoelectron spectra recorded at 193 (6.424 eV; left column), 266 (4.661 eV; middle column), and 355 nm (3.496 eV, right column) photon energies for (a) $[Fe(mnt)_2]^{2-}$, (b) $[Co(mnt)_2]^{2-}$, (c) $[Ni(mnt)_2]^{2-}$, (d) $[Cu(mnt)_2]^{2-}$, and (e) $[Zn(mnt)_2]^{2-}$. The inset in the 266 nm spectrum of $[Fe(mnt)_2]^{2-}$ is an expansion of the region 0−0.8 eV to illustrate features X and A more clearly. Features marked with an asterisk in the 266 and 355 nm spectrum were not observed at 193 nm and are assumed to be due to autodetachment or multielectron processes.

Table 1. Experimantal Adiabatic (ADE) and Vertical (VDE) Detachment Energies for the Dianions $[M(mnt)_2]^{2-}$ (M = Fe−Zn)[a]

	feature[b]	$[Fe(mnt)_2]^{2-}$	$[Co(mnt)_2]^{2-}$	$[Ni(mnt)_2]^{2-}$	$[Cu(mnt)_2]^{2-}$	$[Zn(mnt)_2]^{2-}$
ADE		0.31(5)	0.41(3)	0.44(4)	0.68(4)	1.33(5)
VDE	X	0.36(5)	0.44(4)	0.49(3)	0.85(5)	1.56(5)
	A	0.64(7)	0.61(4)	1.35(3)	1.20(5)	3.0(1)
	B	0.88(4)	1.17(5)	1.48(3)	1.91(5)	3.57(5)
	C	1.18(4)	1.58(5)	1.90(3)		

[a] The numbers in parentheses represent the uncertainty in the last digit. [b] Refers to the features labeled in Figure 1.

are more clearly resolved in the 266 and 355 nm spectra (Figure 1b). The signal between features A and B at 266 and 355 nm is broad and is likely due to autodetachment transitions.

$[Ni(mnt)_2]^{2-}$. The spectra for $[Ni(mnt)_2]^{2-}$ have been reported previously in comparison with the heavier Pd and Pt congeners[18] but are included here again for the sake of completeness and for comparison with the remaining $[M(mnt)_2]^{2-}$ centers. The features labeled A, B in the 193 nm spectrum were resolved into two distinct features in the 266 and 355 nm spectra (Figure 1c). The signal between features X, A and B, C at 266 and 355 nm is broad and was assigned to autodetachment transitions.

$[Cu(mnt)_2]^{2-}$. The VDE of feature X was 0.85 eV, which is higher than that for the Fe−Ni centers described above (Table 1). The difference between the VDE and ADE of 0.17 eV is also larger than that for the Fe−Ni centers (Table 1). Two additional features labeled A and B were observed at 1.20 and 1.91 eV, respectively.

$[Zn(mnt)_2]^{2-}$. The spectra of $[Zn(mnt)_2]^{2-}$ appear simpler, with only three features observed at 193 nm (Figure 1). The first detachment feature occurred with a VDE of 1.56 eV, which is significantly higher than that for the Fe−Cu centers (Table 1). The difference between the VDE and ADE of 0.23 eV is larger than that for $[Cu(mnt)_2]^{2-}$ and much larger than that for the equivalent Fe−Ni centers (Table 1). The two broader features at higher binding energies (A, B) were centered at 3.0 and 3.57 eV. The 266 nm spectrum contained a very broad feature centered at ∼2.2 eV that was not present in the 193 nm spectrum and is assigned to an autodetachment transition.

Photoelectron Spectra of the Singly Charged Anions $[M(mnt)_2]^{1-}$ (M = Fe, Co, Ni, Cu). The binding energies of the monoanions $[M(mnt)_2]^{1-}$ were significantly higher than those for the dianions due to the absence of Coulomb repulsion in the former. This meant that the 266 nm photons were of insufficient energy to detach electrons from $[M(mnt)_2]^{1-}$ and that spectra could only be recorded at 193 nm (Figure 2). The first few detachment features for each $[M(mnt)_2]^{1-}$ are again labeled X, A, B, etc. in order of increasing binding energies, and their ADEs and VDEs are detailed in Table 2.

$[Fe(mnt)_2]^{1-}$. Feature X was well resolved and separated from feature A by ∼0.7 eV. The relative intensity of this first feature is much higher than the weak threshold features observed for $[Fe(mnt)_2]^{2-}$ (Figure 1a). There is continuous electron signal in the region 5.4−5.9 eV, which is presumably due to the superposition of multiple detachment transitions.

$[Co(mnt)_2]^{1-}$. The first and second features occur at very similar energies and are separated by only 0.13 eV. The small separation between these features appeared similar to that observed for the first two features for $[Co(mnt)_2]^{2-}$ (Figure 1b). The region between 5.4 and 6.0 eV is again very congested.

$[Ni(mnt)_2]^{1-}$. Features X and A were separated by ∼0.8 eV. Two stronger features were apparent in the region 5.5−6.0 eV; however, the signal is not resolved to the baseline and additional weaker features are likely obscured.

$[Cu(mnt)_2]^{1-}$. Only two features labeled X and A and separated by ∼0.8 eV were observed. The difference between the VDE and ADE of 0.04 eV is less than that for $[Cu(mnt)_2]^{2-}$ (0.17 eV) and similar to that for the other $[M(mnt)_2]^{1-}$ centers (Table 2).

Theoretical Results. Each of $[M(mnt)_2]^{2-}$ (M = Fe−Ni) and $[M(mnt)_2]^{1-}$ (M = Fe−Cu) was calculated as having planar geometries of D_{2h} point symmetry, consistent with available solid-state data.[40] In contrast, $[Cu(mnt)_2]^{2-}$ and $[Zn(mnt)_2]^{2-}$ were predicted to have nonplanar geometries of lower D_2 and D_{2d} point symmetry, respectively, with dihedral angles between the two dithiolene ligands of 31° and 90°. The D_2 geometry for $[Cu(mnt)_2]^{2-}$ was favored over the planar D_{2h} geometry by only 0.06 eV, which is consistent with some (but not all) crystal structures of $[Cu(mnt)_2]^{2-}$ exhibiting similar deviations from planarity.[40−42] The calculated geometry for $[Zn(mnt)_2]^{2-}$ is consistent with that expected on the basis of the d^{10} configuration and that observed in the solid state.[40]

The ground-state electronic structure for each of $[M(mnt)_2]^{n-}$ was chosen with guidance from available condensed-phase data and from the theoretical calculations. $[Zn(mnt)_2]^{2-}$ has

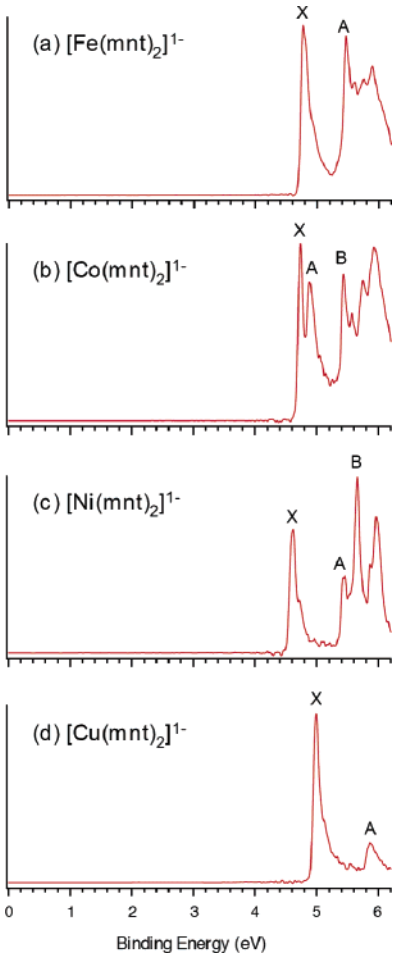

Figure 2. Photoelectron spectra recorded at 193 nm (6.424 eV) photon energy for (a) $[Fe(mnt)_2]^{1-}$, (b) $[Co(mnt)_2]^{1-}$, (c) $[Ni(mnt)_2]^{1-}$, and (d) $[Cu(mnt)_2]^{1-}$.

Table 2. Experimental Vertical (VDE) and Adiabatic (ADE) Detachment Energies for the Monoanions $[M(mnt)_2]^{1-}$ (M = Fe−Cu)[a]

	feature[b]	$[Fe(mnt)_2]^{1-}$	$[Co(mnt)_2]^{1-}$	$[Ni(mnt)_2]^{1-}$	$[Cu(mnt)_2]^{1-}$
ADE		4.74(3)	4.70(3)	4.58(3)	4.96(4)
VDE	X	4.77(3)	4.74(3)	4.62(3)	5.00(3)
	A	5.47(3)	4.87(4)	5.43(4)	5.84(5)
	B	5.90(5)	5.44(4)	5.66(3)	

[a] The numbers in parentheses represent the uncertainty in the last digit. [b] Refers to the features labeled in Figure 2.

(40) Beswick, C. L.; Schulman, J. M.; Stiefel, E. I. Structures and Structural Trends in Homoleptic Dithiolene Complexes. In *Progress in Inorganic Chemistry*; Karlin, K. D., Series Ed.; Wiley: New York, 2003; Vol. 52, p 55.
(41) Snaathorst, D.; Doesburg, H. M.; Perenboom, J. A. A. J.; Keijzers, C. P. *Inorg. Chem.* **1981**, *20*, 2526.
(42) Kuppusamy, P.; Manoharan, P. T. *Inorg. Chem.* **1985**, *24*, 3053.

a d^{10} configuration and is diamagnetic.[43] The dianion $[Cu(mnt)_2]^{2-}$ has a doublet ground state, while the singly charged anion $[Cu(mnt)_2]^{1-}$ is diamagnetic.[44] $[Ni(mnt)_2]^{2-}$ and $[Ni(mnt)_2]^{1-}$ are both well characterized with singlet and doublet ground states, respectively.[6,43−48] $[Co(mnt)_2]^{2-}$ has a doublet ground state.[47,49] $[Co(mnt)_2]^{1-}$ crystallizes as binuclear $[Co_2(mnt)_4]^{2-}$ in the solid state and is diamagnetic but dissociates in solution to form mononuclear solvated complexes with either singlet or triplet ground states, dependening on the solvent and number of coordinated solvent molecules.[44,50,51] The calculations predicted that singlet and triplet states of $[Co(mnt)_2]^{1-}$ were degenerate, and so both cases were considered when interpreting the photoelectron spectrum of $[Co(mnt)_2]^{1-}$. $[Fe(mnt)_2]^{2-}$ is predicted to have a triplet ground state, consistent with that observed for related species $[Fe(L)_2]^{2-}$ (L = bdt = benzene-1,2-dithiolato or related ligand).[13,52,53] The monoanion $[Fe(mnt)_2]^{1-}$ also crystallizes as binuclear $[Fe_2(mnt)_4]^{2-}$ in the solid state[54] but exhibits a quartet ground state in solution,[44] and calculations indicated this was also favored in the gas phase.

The calculated first VDEs for each of $[M(mnt)_2]^{n-}$ for vertical electron detachment from the ground state of the parent species to the ground state of the product species are detailed in Table 3. The calculations predicted the lowest energy singlet and triplet states of $[Co(mnt)_2]^{1-}$ to be very similar in energy, and so VDEs for electron detachment from doublet $[Co(mnt)_2]^{2-}$ to access both these states are included in Table 3. Similarly, the first VDEs for electron detachment from both these states to access neutral $[Co(mnt)_2]$ are also included.

MO energy levels and contour plots for occupied orbitals within ~1.5 eV of the highest energy occupied orbital for each of $[M(mnt)_2]^{n-}$ are presented in Figures 3−7. Detachment from these frontier orbitals should give rise to the detachment features that are labeled in the photoelectron spectra of Figures 1 and 2.

Discussion

Spectral Assignment for $[M(mnt)_2]^{2-}$ and $[M(mnt)_2]^{1-}$. Detachment features in the photoelectron spectra of $[M(mnt)_2]^{n-}$ arise from transitions from the ground states of the parent species to the ground and excited states of the one-electron detached species. Therefore, the photoelectron spectra of Figures 1 and 2 provide information about the relative energies of the ground and excited states of $[M(mnt)_2]^{1-}$ and $[M(mnt)_2]$. Alternatively, within the single particle approximation of Koopmans' theorem, these detachment features can also be viewed as arising from the direct ionization of electrons from occupied orbitals of the parent species, thereby providing direct information about their MO energy levels. The spectra of Figures 1 and 2 were qualitatively interpreted using the predicted MO energy levels for $[M(mnt)_2]^{2-}$ and $[M(mnt)_2]^{1-}$ from the DFT calculations (Figures 3−7). The spectra for $[Ni(mnt)_2]^{2-}$ and $[Ni(mnt)_2]^{1-}$ are discussed first, as these have been presented previously,[18] and the dianion is a closed-shell species which makes interpretation simpler. These are followed by $[Co(mnt)_2]^{n-}$ and $[Fe(mnt)_2]^{n-}$ which have equivalent planar D_{2h} geometries, and then $[Cu(mnt)_2]^{1-}$, $[Cu(mnt)_2]^{2-}$, and $[Zn(mnt)_2]^{2-}$, which involve an increase in the dihedral angle between the two dithiolene ligands and the transition from D_{2h} to D_2 and then D_{2d} point symmetry, respectively.

Table 3. Theoretical Data for the First VDE for the Anions $[M(mnt)_2]^{2-}$ (M = Fe−Zn) and $[M(mnt)_2]^{1-}$ (M = Fe−Cu)[a]

transition	orbital[b]	VDE (eV) calcd	VDE (eV) exptl
Dianions			
$[Fe(mnt)_2]^{2-}$ ($^3B_{1g}$) → $[Fe(mnt)_2]^{1-}$ ($^4B_{1g}$)	β78 a_g	0.36	0.36
$[Co(mnt)_2]^{2-}$ ($^2B_{2g}$) → $[Co(mnt)_2]^{1-}$ ($^3B_{1g}$)	β79 b_{3g}	0.54	0.44
$[Co(mnt)_2]^{2-}$ ($^2B_{2g}$) → $[Co(mnt)_2]^{1-}$ (^1A_g)	α80 b_{2g}	0.59	
$[Ni(mnt)_2]^{2-}$ (^1A_g) → $[Ni(mnt)_2]^{1-}$ ($^2B_{2g}$)	80 b_{2g}	0.37	0.49
$[Cu(mnt)_2]^{2-}$ ($^2B_1$) → $[Cu(mnt)_2]^{1-}$ ($^1A_1$)	α81 b_1	0.83	0.85
$[Zn(mnt)_2]^{2-}$ ($^1A_1$) → $[Zn(mnt)_2]^{1-}$ [c]	81,80 e	1.11	1.56
Monoanions			
$[Fe(mnt)_2]^{1-}$ ($^4B_{1g}$) → $[Fe(mnt)_2]$ ($^3B_{3g}$)	α80 b_{2g}	4.64	4.77
$[Co(mnt)_2]^{1-}$ ($^3B_{1g}$) → $[Co(mnt)_2]$ ($^2B_{3g}$)	α80 b_{2g}	4.64	4.74
$[Co(mnt)_2]^{1-}$ (^1A_g) → $[Co(mnt)_2]$ ($^2B_{3g}$)	79 b_{3g}	4.62	
$[Ni(mnt)_2]^{1-}$ ($^2B_{2g}$) → $[Ni(mnt)_2]$ (^1A_g)	α80 b_{2g}	4.57	4.62
$[Cu(mnt)_2]^{1-}$ (^1A_g) → $[Cu(mnt)_2]$ ($^2B_{2g}$)	80 b_{2g}	5.08	5.00

[a] Experimental VDEs are included for comparison. [b] Refers to the orbital of the parent species from which the electron is detached (see Figures 3−7). [c] Detachment from the degenerate HOMO of $[Zn(mnt)_2]^{2-}$ results in a Jahn−Teller effect in product $[Zn(mnt)_2]^{1-}$.

Spectral Assignment for $[Ni(mnt)_2]^{2-}$. The dianion $[Ni(mnt)_2]^{2-}$ has a singlet ground state, and so only transitions to doublet $[Ni(mnt)_2]^{1-}$ are possible (Figure 5a). The spectrum of $[Ni(mnt)_2]^{2-}$ has been assigned in detail elsewhere,[18] but is described again briefly for comparison with the other species presented here. The calculated VDE for detachment from the HOMO of $[Ni(mnt)_2]^{2-}$ to access the ground state of $[Ni(mnt)_2]^{1-}$ is 0.37 eV, and is in reasonable agreement with the VDE for feature X of 0.49 eV. The HOMO−1 and HOMO−2 levels are metal-based and are predicted to occur at similar energies and about 0.7−0.9 eV below the HOMO, in agreement with the positions of features A and B at 0.8−1.0 eV higher binding energy than feature X. The HOMO−3 is predicted to occur 1.33 eV below the HOMO, consistent with the position of feature C at 1.4 eV higher binding energy than feature X.

Spectral Assignment for $[Ni(mnt)_2]^{1-}$. The doublet ground state of $[Ni(mnt)_2]^{1-}$ means that transitions to singlet

(43) Billig, E.; Williams, R.; Bernal, I.; Waters, J. H.; Gray, H. B. *Inorg. Chem.* **1964**, *3*, 663.
(44) Williams, R.; Billig, E.; Waters, J. H.; Gray, H. B. *J. Am. Chem. Soc.* **1966**, *88*, 43.
(45) Davison, A.; Edelstein, N.; Holm, R. H.; Maki, A. H. *Inorg. Chem.* **1963**, *2*, 1227.
(46) Davison, A.; Edelstein, N.; Holm, R. H.; Maki, A. H. *J. Am. Chem. Soc.* **1963**, *85*, 2029.
(47) Maki, A. H.; Edelstein, N.; Davison, A.; Holm, R. H. *J. Am. Chem. Soc.* **1964**, *86*, 4580.
(48) Huyett, J. E.; Choudhury, S. B.; Eichhorn, D. M.; Bryngelson, P. A.; Maroney, M. J.; Hoffman, B. M. *Inorg. Chem.* **1998**, *37*, 1361.
(49) Davison, A.; Edelstein, N.; Holm, R. H.; Maki, A. H. *J. Am. Chem. Soc.* **1963**, *85*, 3049.
(50) Bray, J.; Locke, J.; McCleverty, J. A.; Coucouvanis, D. *Inorg. Synth.* **1967**, *13*, 187.
(51) Dance, I. G.; Miller, T. R. *Inorg. Chem.* **1974**, *13*, 525.
(52) Sellmann, D.; Kleinekleffmann, U.; Zapf, L.; Huttner, G.; Zsolnai, L. *J. Organomet. Chem.* **1984**, *263*, 321.
(53) Sellmann, D.; Geck, M.; Moll, M. *J. Am. Chem. Soc.* **1991**, *113*, 5259.
(54) Hamilton, W. C.; Bernal, I. *Inorg. Chem.* **1967**, *6*, 2003.

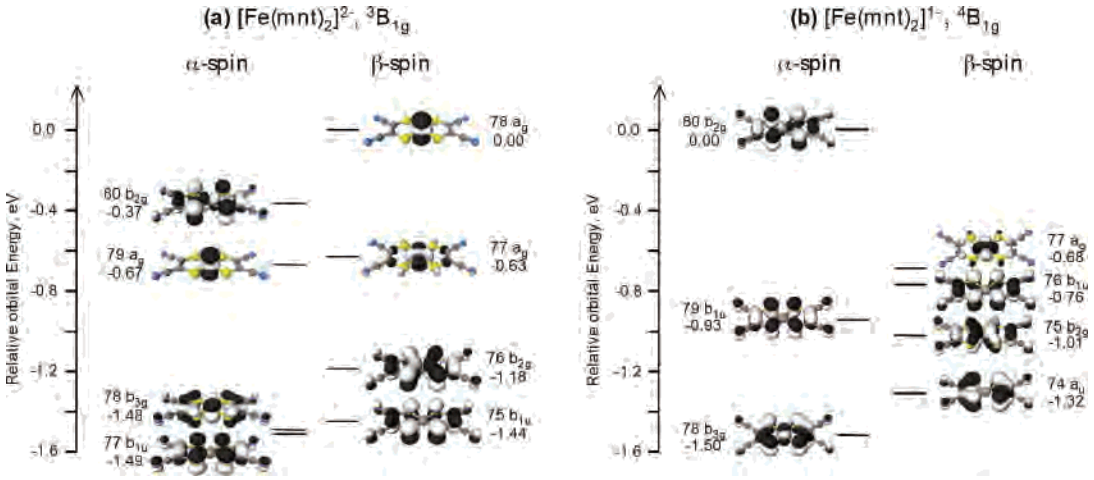

Figure 3. Kohn−Sham orbital pictures and energies (eV, relative to the HOMO) for the highest energy occupied orbitals of (a) $^3B_{1g}[Fe(mnt)_2]^{2-}$ and (b) $^4B_{1g}[Fe(mnt)_2]^{1-}$. The $^3B_{1g}$ ground state of $[Fe(mnt)_2]^{2-}$ arises because the β-spin−orbitals corresponding to α80 b_{2g} and α78 b_{3g} are vacant. Electron detachment from the β-spin−orbital β78 a_g of $[Fe(mnt)_2]^{2-}$ gives rise to the $^4B_{1g}$ ground state of product $[Fe(mnt)_2]^{1-}$.

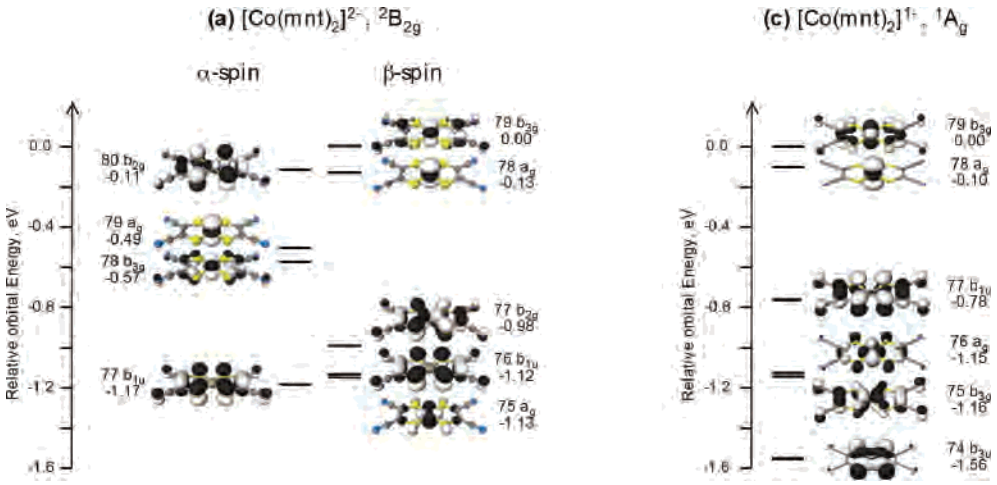

Figure 4. Kohn−Sham orbital pictures and energies (eV, relative to the HOMO) for the highest energy occupied orbitals of (a) $^2B_{2g}[Co(mnt)_2]^{2-}$ and (b) $^1A_g[Co(mnt)_2]^{1-}$. The $^2B_{2g}$ ground state of $[Co(mnt)_2]^{2-}$ arises because the β-spin−orbitals corresponding to α80 b_{2g} are vacant. Electron detachment from the α-spin−orbital β80 b_{2g} of $[Co(mnt)_2]^{2-}$ gives rise to the ^1A_g ground state of product $[Co(mnt)_2]^{1-}$.

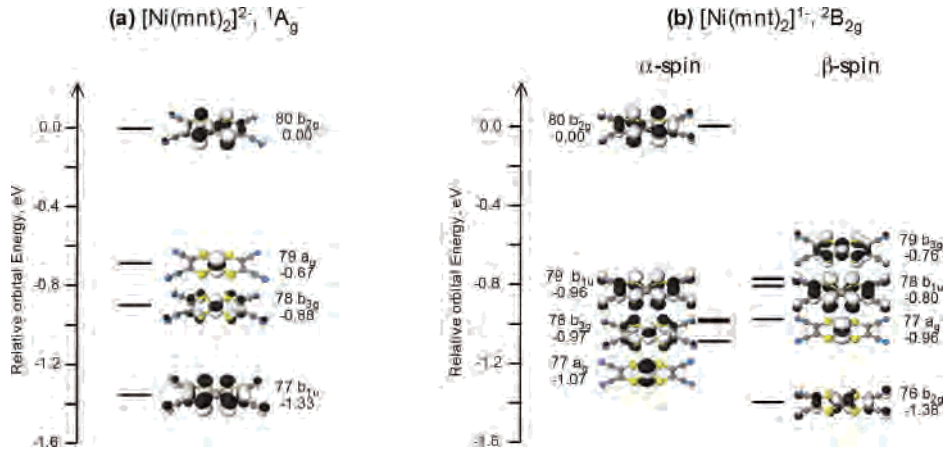

Figure 5. Kohn−Sham orbital pictures and energies (eV, relative to the HOMO) for the highest energy occupied orbitals of (a) $^1A_g[Ni(mnt)_2]^{2-}$ and (b) $^2B_{2g}[Ni(mnt)_2]^{1-}$. Electron detachment from the doubly occupied orbital 80 b_{2g} of $[Ni(mnt)_2]^{2-}$ gives rise to the $^2B_{2g}$ ground state of product $[Ni(mnt)_2]^{1-}$.

and triplet states of neutral $[Ni(mnt)_2]$ are possible (Figure 5b). The HOMO of $[Ni(mnt)_2]^{1-}$ is the highest energy occupied α-spin−orbital, α80 b_{2g}. Detachment from this orbital to access the ^1A_g ground state of neutral $[Ni(mnt)_2]$ is predicted to occur at 4.57 eV, in good agreement with the VDE for feature X of 4.62 eV (Table 3). The orbital energy diagram indicated that the HOMO is clearly separated from deeper lying orbitals by ∼0.8 eV (Figure 5b), consistent with the experimental separation between features X and A of 0.81 eV. The calculations predicted a high density of orbitals

from ~0.8−1.4 eV below the HOMO, which indicated a number of detachment transitions should occur in the region 5.4−6.0 eV. Three strong features were apparent in this region; however, the signal is not resolved to the baseline and additional features of weaker intensity are likely to be obscured. The high density of orbitals predicted in this region prevents a more detailed assignment of these features.

Spectral Assignment for $[Co(mnt)_2]^{2-}$. The dianion $[Co(mnt)_2]^{2-}$ has a doublet ground state, meaning that transitions to singlet and triplet states of $[Co(mnt)_2]^{1-}$ are possible (Figure 4a). The orbital energy diagram indicated that the three highest energy occupied orbitals occurred at very similar energies (within 0.13 eV), in qualitative agreement with the close spacing between features X and A observed experimentally (0.17 eV, Figure 1b). The calculations also predicted that detachment to the lowest energy singlet and triplet states of product $[Co(mnt)_2]^{1-}$ should occur at very similar energies (Table 3). Detachment from the highest energy occupied β-spin−orbital (β79 b_{3g}, Figure 4a) to access a triplet state of $[Co(mnt)_2]^{1-}$ was predicted to occur at 0.54 eV, while detachment from the highest energy occupied α-spin−orbital (α80 b_{2g}) to access the lowest energy singlet state of $[Co(mnt)_2]^{1-}$ was predicted to occur at 0.59 eV. These detachment energies are both very similar and in the region of features X and A (Figure 1b, Table 1). These similar energies suggested that singlet and triplet states of $[Co(mnt)_2]^{1-}$ should be very close in energy (see below). The MO energy levels for $[Co(mnt)_2]^{2-}$ suggested that detachment from the orbital β78 a_g should also occur at a very similar energy. Accordingly, features X and A are assigned to a combination of detachment from the levels β79 b_{3g}, β78 a_g, and α80 b_{2g}, but their close spacing prevents a more definitive assignment (Figure 4a). The orbitals α79 a_g and α78 b_{3g} are predicted to occur about 0.5−0.6 eV below the HOMO (Figure 4a) and in agreement with the position of feature B.

Spectral Assignment for $[Co(mnt)_2]^{1-}$. The calculations predicted singlet and triplet states of $[Co(mnt)_2]^{1-}$ at their relaxed geometries to be degenerate. The first VDEs for these states were calculated as 4.62 and 4.64 eV, respectively, which are both in good agreement with the experimental VDE of 4.74 eV (Table 3). However, the predicted MO energy levels for singlet $[Co(mnt)_2]^{1-}$ are in much closer agreement with the experimental data. The calculated MO energy levels for singlet $[Co(mnt)_2]^{1-}$ are presented in Figure 4b, while those for the triplet state are included in the Supporting Information (Figure S1). The HOMO−1 of singlet $[Co(mnt)_2]^{1-}$ is predicted to occur 0.10 eV below the HOMO, in agreement with the small separation between features X and A observed experimentally (0.13 eV, Figure 2b). In contrast, the calculations predicted a large separation of ~0.8 eV between the HOMO and HOMO−1 levels of triplet $[Co(mnt)_2]^{1-}$ (Figure S1), in much poorer agreement with the experimental data. The calculated spacing of 0.68 eV between the HOMO−1 and HOMO−2 levels of singlet $[Co(mnt)_2]^{1-}$ was also consistent with the experimental separation between features A and B of 0.57 eV. This agreement indicated that the ground state of gaseous $[Co(mnt)_2]^{1-}$ is likely to be the singlet state. This assignment differs with the triplet ground state observed for the related species $[Co(bdt)_2]^{1-}$ (bdt = benzene-1,2-dithiolato).[13,55]

Spectral Assignment for $[Fe(mnt)_2]^{2-}$. The triplet ground state of $[Fe(mnt)_2]^{2-}$ means that transitions to doublet and quartet states of $[Fe(mnt)_2]^{1-}$ are possible (Figures 3a). The first two detachment features were considerably weaker than those at higher binding energies (Figure 1a, inset). Similar weak onset features have been observed previously for mononuclear high-spin tetrahedral Fe(II) centers, and in each case were assigned to detachment of the single Fe 3d β-spin electron [e.g., Fe^{II} ($3d^6$) $S = 2 \rightarrow Fe^{III}$ ($3d^5$) $S = {}^5/_2$].[30,56,57] This indicated that the two weak onset features observed for $[Fe(mnt)_2]^{2-}$ might also be due to detachment of the two Fe 3d β-spin electrons.

The calculations indicated that the two highest energy occupied β-spin−orbitals of $[Fe(mnt)_2]^{2-}$ were the metal-based orbitals Fe $3d_{z^2}$ and Fe $d_{x^2-y^2}$ (Figure 3a). The first detachment feature is predicted to arise from detachment from the Fe $3d_{z^2}$ orbital to access the quartet ground state of product $[Fe(mnt)_2]^{1-}$ (Figure 3a). This was predicted to occur at 0.36 eV, in good agreement with the VDE for feature X of 0.36 eV (Table 3). The second detachment feature for $[Fe(mnt)_2]^{2-}$ was also weak, suggesting that it should also arise from a metal-based orbital. However, the calculations indicated the second highest energy occupied orbital for $[Fe(mnt)_2]^{2-}$ was the ligand-based orbital α80 b_{2g}, which is expected to give rise to a strong detachment transition. The third highest energy occupied orbital is the metal-based β-spin−orbital Fe $3d_{x^2-y^2}$ (β77 a_g), and detachment from this orbital should give rise to a weaker detachment feature similar to that observed experimentally (Figure 5a). Accordingly, feature A is assigned to detachment from the β-spin Fe $3d_{x^2-y^2}$ orbital (β77 a_g), while the stronger feature B is assigned to detachment from the ligand-based orbital α80 b_{2g} (Figure 5). These assignments are the reverse of the predicted orbital ordering but provide a more sensible agreement with the intensity of the observed spectral features. The metal-based orbital α79 a_g (Fe $3d_{z^2}$) should also give rise to a weaker detachment feature, which might be obscured by the stronger detachment features B and C.

The observation of two weak threshold detachment features for $[Fe(mnt)_2]^{2-}$ contrasts with the single weak feature observed previously for other Fe(II) centers such as $Fe(SCH3)_3^{1-}$ and $Na^+[Fe(SCN)_4]^{2-}$.[30,56,57] However, these latter species involve high-spin d^6 $S = 2$ centers with only a single Fe 3d β-spin electron. In contrast, square planar $[Fe(mnt)_2]^{2-}$ involves an intermediate spin $S = 1$ d^6 center with two Fe 3d β-spin electrons (Figure 3a). Accordingly, the observation of two weak threshold detachment features for the latter is consistent with the presence of two Fe 3d β-spin electrons.

(55) van der Put, P. J.; Schilperoord, A. A. *Inorg. Chem.* **1974**, *13*, 2476.
(56) Yang, X.; Wang, X. B.; Fu, Y. J.; Wang, L. S. *J. Phys. Chem. A* **2003**, *107*, 1703.
(57) Yang, X.; Wang, X. B.; Wang, L. S.; Niu, S. Q.; Ichiye, T. *J. Chem. Phys.* **2003**, *119*, 8311.

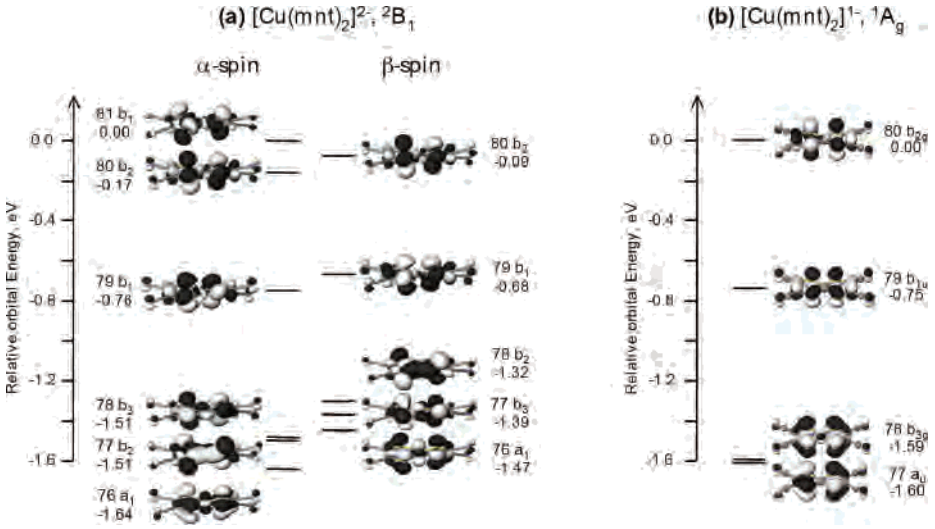

Figure 6. Kohn−Sham orbital pictures and energies (eV, relative to the HOMO) for the highest energy occupied orbitals of (a) $^2B_1[Cu(mnt)_2]^{2-}$ and (b) $^1A_g[Cu(mnt)_2]^{1-}$. The $^2B_1$ ground state of $[Cu(mnt)_2]^{2-}$ arises because the β-spin−orbital corresponding to α81 b_1 is vacant. Electron detachment from the α-spin−orbital β80 b_1 of $[Cu(mnt)_2]^{2-}$ gives rise to the ^1A_g ground state of product $[Cu(mnt)_2]^{1-}$.

Spectral Assignment for [Fe(mnt)$_2$]$^{1-}$. The quartet ground state of $[Fe(mnt)_2]^{1-}$ means that transitions to triplet and quintet states of product $[Fe(mnt)_2]$ are possible (Figure 3b). The first detachment feature for $[Fe(mnt)_2]^{1-}$ exhibited strong intensity, suggesting it should arise from a ligand-based orbital (Figure 2). The highest energy occupied orbital of $[Fe(mnt)_2]^{1-}$ is the ligand-based orbital α80 b_{2g} (Figure 3b). Detachment from this orbital to access the triplet ground state of neutral $[Fe(mnt)_2]$ was predicted to occur at 4.64 eV, in reasonable agreement with the VDE for feature X of 4.77 eV. The predicted separation between the HOMO and deeper lying orbitals of ∼0.7 eV was consistent with the separation between features X and A of 0.70 eV. Again, the calculations predict a high density of orbitals from ∼0.7 to 1.5 eV below the HOMO, consistent with the high spectral density observed at higher binding energy, but preventing a more detailed assignment of these features.

Spectral Assignment for [Cu(mnt)$_2$]$^{2-}$. The calculations predicted $[Cu(mnt)_2]^{2-}$ to exhibit lower D_2 point symmetry with a dihedral angle between the two dithiolene ligands of 31°. The doublet ground-state means that transitions to singlet and triplet states of $[Cu(mnt)_2]^{1-}$ are possible (Figure 6a). Detachment from the HOMO (α81 b_1) to access the singlet ground state of $[Cu(mnt)_2]^{1-}$ was predicted to occur at 0.83 eV, in good agreement with the VDE of feature X of 0.85 eV. The width of feature X (VDE − ADE = 0.17 eV, Table 1) is consistent with detachment from this orbital giving rise to relaxation from the D_2 geometry of $[Cu(mnt)_2]^{2-}$ to the planar D_{2h} geometry of $[Cu(mnt)_2]^{1-}$ (Figure 6). Feature X is closely followed by feature A with a VDE of 1.20 eV, which is assigned to detachment from orbitals α80 b_2 and β80 b_2, which are predicted to occur at similar energies and ∼0.1−0.2 eV below the HOMO. The predicted separation between the 80 b_2 and 79 b_1 levels of ∼0.6 eV was consistent with the separation between features A and B of ∼0.7 eV and suggested that feature B could be assigned to detachment from the α79 b_1 and β79 b_1 levels.

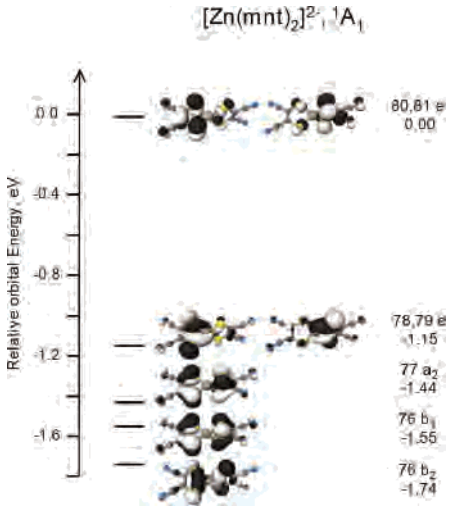

Figure 7. Kohn−Sham orbital pictures and energies (eV, relative to the HOMO) for the highest energy occupied orbitals of $[Zn(mnt)_2]^{2-}$.

Spectral Assignment for [Cu(mnt)$_2$]$^{1-}$. The singlet ground state of $[Cu(mnt)_2]^{1-}$ means that only transitions to doublet states of neutral $[Cu(mnt)_2]$ are possible (Figure 6). The VDE for detachment from the HOMO to access the ground state of neutral $[Cu(mnt)_2]$ is calculated as 5.08 eV, in good agreement with the VDE for feature X of 5.00 eV. The HOMO−1 is predicted to occur 0.75 eV below the HOMO, in agreement with the experimental separation between features X and A of 0.84 eV. The HOMO−2 and HOMO−3 levels are predicted to occur ∼1.6 eV below the HOMO, suggesting that detachment from these levels should occur at ∼6.6 eV. This is higher than the photon energy used in the experiment (193 nm, 6.424 eV) and is consistent with detachment from these levels not being observed.

Spectral Assignment for [Zn(mnt)$_2$]$^{2-}$. The d^{10} configuration means that this dianion exhibits D_{2d} symmetry with a singlet ground state (Figure 7). Detachment from the doubly degenerate HOMO is predicted to occur at 1.11 eV, which is below the experimental VDE of 1.56 eV, and indicates

that the stability of $[Zn(mnt)_2]^{2-}$ is underestimated in the present calculations. Detachment from the doubly degenerate HOMO of $[Zn(mnt)_2]^{2-}$ should give rise to a Jahn−Teller effect in product $[Zn(mnt)_2]^{1-}$ and result in distortion to a lower D_2 geometry similar to that of $[Cu(mnt)_2]^{2-}$ (Figure 6a). This geometric relaxation is consistent with the larger width of feature X for $[Zn(mnt)_2]^{2-}$ (VDE − ADE = 0.23 eV) relative to the equivalent Fe, Co, and Ni centers which are not expected to undergo similar geometry changes (Table 1). The HOMO and HOMO−1 of $[Zn(mnt)_2]^{2-}$ are separated by 1.15 eV, in qualitative agreement with the separation between features X and A of 1.4 eV. The HOMO−2 to HOMO−4 are predicted to lie directly below the HOMO−1 and should contribute to features A and B.

Changes in Electronic Structure Across the Series $[M(mnt)_2]^{n-}$. The combined experimental and theoretical data provide a detailed picture of the MO energy levels of the series $[M(mnt)_2]^{n-}$ and insights into changes in the energies and relative ordering of frontier orbitals between different species. In particular, comparisons between the doubly and singly charged anions of the same metal center allows for the effect of oxidation on the relative energies of frontier orbitals to be examined. Similarly, comparisons between species of the same charge but different metal center allows for the effect of metal center and change in coordination geometry to be examined.

Effect of Charge State on Electronic Structure. $[Fe(mnt)_2]^{2-}$ and $[Fe(mnt)_2]^{1-}$. The first two features for the dianion $[Fe(mnt)_2]^{2-}$ were assigned to the β-spin−orbitals Fe $3d_{z^2}$ and Fe $3d_{x^2-y^2}$, respectively (Figure 3a). In contrast, the first detachment feature for $[Fe(mnt)_2]^{1-}$ was assigned to a ligand-based orbital (α80 b_{2g}), with the first metal-based feature at least 0.7 eV higher in energy (Figure 3b). These differences demonstrate the stabilization of Fe 3d levels from ferrous $[Fe(mnt)_2]^{2-}$ to ferric $[Fe(mnt)_2]^{1-}$ and are consistent with similar stabilization of Fe 3d levels demonstrated for the related centers $[FeCl_4]^{2-/1-}$ and $[Fe(SR)_4]^{2-/1-}$ by ligand K-edge X-ray absorption spectroscopy.[58−61] The assignment of the first detachment features for $[Fe(mnt)_2]^{2-}$ and $[Fe(mnt)_2]^{1-}$ as arising from metal- and ligand-based orbitals, respectively, also supports recent descriptions of the electronic structure of the three-member electron-transfer series $[Fe(bdt)_2]^{n-}$ (bdt = benzene-1,2-dithiolato; n = 0−2) as $[Fe^{II}(bdt)_2]^{2-} \rightarrow [Fe^{III}(bdt)_2]^{1-} \rightarrow [Fe^{III}(bdt^{\bullet})(bdt)]$.[12] In particular, the present experiments clearly demonstrate that the ground state of neutral $[Fe(mnt)_2]$ does not involve an Fe^{IV} center, with the separation between features X and A for $[Fe(mnt)_2]^{1-}$ indicating that an $[Fe^{IV}(mnt)_2]$ configuration is at least 0.7 eV higher in energy than the $[Fe^{III}(mnt^{\bullet})(mnt)]$ ground state.

$[Ni(mnt)_2]^{2-}$ and $[Ni(mnt)_2]^{1-}$. The first detachment feature for both of $[Ni(mnt)_2]^{2-}$ and $[Ni(mnt)_2]^{1-}$ was assigned to detachment from the same ligand-based orbital in both cases (80 b_{2g}, Figure 5), in contrast with the situation described above for $[Fe(mnt)_2]^{n-}$. These differences arise because the Ni 3d orbitals are stabilized relative to the highest energy occupied ligand-based orbitals for both of $[Ni(mnt)_2]^{2-}$ and $[Ni(mnt)_2]^{1-}$, and so oxidation is ligand-based in both cases. These assignments are consistent with the accepted description of the three-member electron-transfer series $[Ni(S_2C_2R_2)]^{2-} \leftrightarrow [Ni(S_2C_2R_2)]^{1-} \leftrightarrow [Ni(S_2C_2R_2)]$ as involving ligand-based redox chemistry in each stage.[6,9,14]

$[Co(mnt)_2]^{2-}$ and $[Co(mnt)_2]^{1-}$. The situation for the cobalt dianion $[Co(mnt)_2]^{2-}$ is intermediate between that of $[Fe(mnt)_2]^{2-}$ and $[Ni(mnt)_2]^{2-}$, with the frontier metal- and ligand-based orbitals occurring at very similar energies (Figure 4a).[13,62] This was supported by the experimental spectra, with detachment features X and A occurring at similar energies and assigned to a combination of detachment from the highest energy occupied metal- and ligand-based orbitals.

$[Cu(mnt)_2]^{2-}$ and $[Cu(mnt)_2]^{1-}$. Feature X for $[Cu(mnt)_2]^{2-}$ was assigned to the orbital α81 b_1. This orbital is vacant for $[Cu(mnt)_2]^{1-}$, and so an equivalent feature was not observed. Features A and B for $[Cu(mnt)_2]^{2-}$ were separated by ∼0.7 eV and were assigned to the doubly occupied levels 80 b_2 and 79 b_1, respectively. Detachment from the equivalent orbitals of $[Cu(mnt)_2]^{1-}$ (80b_{2g} and 79b_{1u}, respectively) were assigned to features X and A, respectively, which were separated by ∼0.8 eV. The similar separation between these orbitals for $[Cu(mnt)_2]^{2-}$ and $[Cu(mnt)_2]^{1-}$ indicated little change in their relative energies with oxidation, consistent with the theoretical predictions (Figure 6).

Effect of the Metal Center on Electronic Structure. $[Fe(mnt)_2]^{2-}$, $[Co(mnt)_2]^{2-}$, and $[Ni(mnt)_2]^{2-}$. These dianions all involve formally M(II) centers in planar D_{2h} geometries with dianionic dithiolene ligands. Detachment features assigned to the M $3d_{z^2}$ orbital were identified in each case and occurred at 0.36, ∼0.6, and 1.35 eV for M = Fe, Co, and Ni, respectively. This increase in binding energy across the series is consistent with stabilization of the M 3d manifold across the series due to the increased effective nuclear charge (Z_{eff}) from Fe^{2+} to Ni^{2+}. Similar stabilization of M 3d levels has been demonstrated for the metal chlorides MCl_4^{2-} and metal thiolates $M(SR)_4^{2-}$ (M = Fe−Cu) by ligand K-edge X-ray absorption spectroscopy.[58,60,61,63] In contrast, the energy of the first ligand-based detachment feature was reduced across the series and occurred at 0.88, ∼0.6, and 0.49 eV, respectively, for M = Fe−Ni. This stabilization and destabilization of metal- and ligand-based features, respectively, meant that the first vertical detachment feature for each of the dianions $[M(mnt)_2]^{2-}$ (M = Fe, Co,

(58) Shadle, S. E.; Hedman, B.; Hodgson, K. O.; Solomon, E. I. *J. Am. Chem. Soc.* **1995**, *117*, 2259.
(59) Rose, K.; Shadle, S. E.; Eidsness, M. K.; Kurtz, D. M.; Scott, R. A.; Hedman, B.; Hodgson, K. O.; Solomon, E. I. *J. Am. Chem. Soc.* **1998**, *120*, 10743.
(60) Glaser, T.; Hedman, B.; Hodgson, K. O.; Solomon, E. I. *Acc. Chem. Res.* **2000**, *33*, 859.
(61) Solomon, E. I.; Hedman, B.; Hodgson, K. O.; Dey, A.; Szilagui, R. K. *Coord. Chem. Rev.* **2005**, *249*, 97.
(62) Bill, E.; Bothe, E.; Chaudhuri, P.; Chlopek, K.; Herebian, D.; Kokatam, S.; Ray, K.; Weyhermüller, T.; Neese, F.; Wieghardt, K. *Chem. Eur. J.* **2005**, *11*, 204.
(63) Rose Williams, K.; Hedman, B.; Hodgson, K. O.; Solomon, E. I. *Inorg. Chim. Acta* **1997**, *263*, 315.

Ni) occurred at very similar binding energies but originated from a different orbital in each case (Figures 3−5).

$[Ni(mnt)_2]^{2-}$ and $[Zn(mnt)_2]^{2-}$. These exhibit D_{2h} and D_{2d} geometries, respectively, with dihedral angles between dithiolene ligands of 0° and 90°. Comparison between the VDEs for related orbitals in the two species allows the effect of this geometry change on their energies to be evaluated. The VDE for detachment from the HOMO of $[Zn(mnt)_2]^{2-}$ was 1.56 eV, which is significantly higher than that of 0.49 eV for the HOMO of $[Ni(mnt)_2]^{2-}$ (Table 1). The HOMO of $[Zn(mnt)_2]^{2-}$ is the doubly degenerate level 80,81 e that is localized on the π framework of one dithiolene ligand and is very similar to the highest energy occupied π orbital of the free dithiolene ligand (Figure 7).[7,14] The equivalent orbitals for $[Ni(mnt)_2]^{2-}$ are split under D_{2h} point symmetry and involve symmetric and asymmetric combinations of this same π orbital which transform as b_{1u} and b_{2g}, respectively (Figure 5a, 77 b_{1u} and 80 b_{2g}). The b_{2g} level is destabilized due to ligand−ligand antibonding interactions and the presence of antibonding M $3d_{xz}$ character. Neither of the destabilizing effects are present for the HOMO of $[Zn(mnt)_2]^{2-}$, and consequently, the VDE of this orbital is much higher. In contrast, the b_{1u}-symmetric combination for $[Ni(mnt)_2]^{2-}$ is stabilized by ligand−ligand bonding interactions (77 b_{1u}, Figure 5a) which are not present in the HOMO of $[Zn(mnt)_2]^{2-}$ (Figure 7). Accordingly, the VDE for the 77 b_{1u} level of $[Ni(mnt)_2]^{2-}$ was 1.90 eV, which is ∼0.35 eV higher than that for the HOMO of $[Zn(mnt)_2]^{2-}$.

The separation between the b_{2g} and b_{1u} orbitals for $[Ni(mnt)_2]^{2-}$ can be compared with that between equivalent orbitals in the isoelectronic species $[Cu(mnt)_2]^{1-}$ (Figure 6b). These were separated by 0.84 eV for $[Cu(mnt)_2]^{1-}$ (features X and A), which is much less than that of 1.41 eV for $[Ni(mnt)_2]^{2-}$ (features X and C). This smaller separation is consistent with the presence of less Cu $3d_{xz}$ antibonding character in the b_{2g} orbital for $[Cu(mnt)_2]^{1-}$ and consequently less destabilization relative to the b_{1u} level, i.e., reduced separation (Figure 6b). These conclusions are supported by recent calculations for the related species $[Ni(bdt)_2]^{2-}$ and $[Cu(bdt)_2]^{1-}$ (bdt = benzene-1,2-dithiolato) which indicated 52% M $3d_{xz}$ character in the b_{2g} level for $[Ni(L)_2]^{2-}$ compared with only 11% for $[Cu(L)_2]^{1-}$.[14] These differences arise from stabilization of the Cu 3d manifold in $[Cu(mnt)_2]^{1-}$ relative to that of Ni 3d in $[Ni(mnt)_2]^{2-}$. Such stabilization is also apparent in the position of other detachment features in the photoelectron spectra: metal-based features were observed between the b_{2g} and b_{1u} levels for $[Ni(mnt)_2]^{2-}$ (A, B) but were not observed for $[Cu(mnt)_2]^{1-}$ and were predicted to occur at much higher binding energy (∼2.7 eV below the HOMO, data not shown).

Conclusions

The electronic structures of the bis(dithiolene) anions $[M(mnt)_2]^{n-}$ (M = Fe−Zn; n = 1, 2) were examined by a combination of photodetachment PES and DFT calculations. The combined data illustrate the changes in relative energies of metal- and ligand-based orbitals across the series $[M(mnt)_2]^{n-}$ with variation of metal (M = Fe−Zn), with charge state (n = 1, 2) and with changes in coordination geometry ($D_{2h} \rightarrow D_{2d}$). Detachment features from metal-based orbitals were observed to shift to higher binding energy from Fe → Ni, consistent with the expected stabilization of M 3d orbitals across the series. These changes resulted in the first vertical detachment feature for each of $[M(mnt)_2]^{2-}$ (M = Fe, Co, Ni) occurring at very similar energies but from a different orbital in each case.

Detachment features due to the frontier dithiolene ligand π orbitals were clearly identified for each $[Ni(mnt)_2]^{2-}$, $[Zn(mnt)_2]^{2-}$, and $[Cu(mnt)_2]^{1-}$. The separation between the symmetric and asymmetric combination (b_{1u} and b_{2g}, respectively) for $[Ni(mnt)_2]^{2-}$ was ∼0.6 eV larger than that for $[Cu(mnt)_2]^{1-}$, consistent with the presence of more Ni $3d_{xz}$ antibonding character in the b_{2g} level (greater destabilization). Comparison between equivalent orbitals for $[Ni(mnt)_2]^{2-}$ (D_{2h}) and $[Zn(mnt)_2]^{2-}$ (D_{2d}) provided qualitative insights into the effects of ligand−ligand and M $3d_{xz}$−ligand interactions on the energies of these levels.

Changes in the relative energies of metal- and ligand-based orbitals with oxidation were largely dependent on the nature of the redox active orbital in the couple $[M(mnt)_2]^{2-/1-}$. Significant differences were observed from $[Fe(mnt)_2]^{2-}$ to $[Fe(mnt)_2]^{1-}$ due to oxidation involving a metal based orbital ($Fe^{II} \rightarrow Fe^{III}$) and the consequent stabilization of Fe 3d levels in the latter. In contrast, the first detachment feature for both of $[Ni(mnt)_2]^{2-}$ and $[Ni(mnt)_2]^{1-}$ originated from the same ligand-based orbital in both cases, a result of Ni 3d orbitals being stabilized relative those of Fe 3d and occurring below the highest energy occupied ligand-based orbital for both of $[Ni(mnt)_2]^{2-}$ and $[Ni(mnt)]^{1-}$ (Figure 5).

The combined data provide insights into changes in the electronic structure across the series $[M(mnt)_2]^{2-/1-}$ (M = Fe−Zn) and highlight changes as a function of metal center, charge state, and coordination geometry. The present results should aid with an interpretation of the solution-phase properties of this important class of species and provides fundamental gas-phase electronic data for comparison with future theoretical calculations.

Acknowledgment. This work was supported by the National Science Foundation (CHE-0349426) and the John Simon Guggenheim Foundation and performed at the W. R. Wiley Environmental Molecular Sciences Laboratory (EMSL), a national scientific user facility sponsored by DOE's Office of Biological and Environmental Research and located at Pacific Northwest National Laboratory, which is operated for the DOE by Battelle. Calculations were performed using the EMSL Molecular Science Computing Facility (MSCF).

Supporting Information Available: Cartesian coordinates and energies for the optimized geometries of $[M(mnt)_2]^{2-}$ and $[M(mnt)_2]^{1-}$ (Table S1−S5); MO energy levels and pictures for the lowest energy triplet state of $[Co(mnt)_2]^{1-}$ (Figure S1); and complete lists of authors for refs 26 and 27. This material is available free of charge via the Internet at http://pubs.acs.org.

IC060255Z